Electronic Supplementary Material (ESI) for Journal of Materials Chemistry A.
This journal is © The Royal Society of Chemistry 2022

Large-scale production of low-cost molybdenum dioxide-phosphide seamless electrode for high-current-density hydrogen evolution

Chuanyong Jian [a,b], Qian Cai [a], Wenting Hong [a]*, and Wei Liu [a,b] *

CAS Key Laboratory of Design and Assembly of Functional Nanostructures, and Fujian Provincial Key Laboratory of Nanomaterials, Fujian Institute of Research on the Structure of Matter, Chinese Academy of Sciences, Fuzhou, Fujian, 350002, PR China

University of Chinese Academy of Sciences, Beijing, 100049, PR China

E-mail: hongwenting@ fjirsm.ac.cn, liuw@fjirsm.ac.cn

Structural characterizations

Scanning electron microscopy (HITACHI UHR FE-SEM SU8010) is employed to characterize the morphologies of the as-grown samples. Transmission electron microscopy (TEM), high-resolution TEM (HRTEM), and energy dispersive X-ray spectroscopy (EDS) mapping studies are conducted on a probe-corrected transmission electron microscope operating at 200 kV (FEI Titan F20 TEM). X-ray photoelectron spectroscopy (XPS) measurements are carried out by a ESCALAB 250Xi system (Thermo Fisher), equipped with a 100 W Al Kα source on a spot size of 100 μm at a 45° incident angle. The binding energy scan ranges from 0 to 1200 eV with an interval step of 1 eV, high-intensity excitation is provided by monochromatic Al Kα X-rays that are 1486.6 eV in energy with a 0.48 eV resolution at full width at half-maximum. The binding energy scale is calibrated to carbon line of 284.8 eV. All XPS spectra are recorded with a resolution of 50 meV. Each data set is first corrected for the nonlinear emission background. The data is then fitted with Gaussian function to find the deconvoluted peak positions. X-ray diffraction (XRD) spectra are obtained to detect the phase of samples using the D8 ADVANCE diffractometer with Cu Kα radiation (λ = 1.5418 Å). The CAs of droplets on the sample

surfaces are recorded by a contact angle measuring device (MDTC-EQ-M07-01, Japan). The droplet volume is the same in each case.

Theoretical Calculations

Density functional theory calculations were carried out in Atomistix Tool Kit 2019.[1] with the Perdew–Burke–Ernzerhof exchange-correlation within the generalized gradient approximation. A 4 × 4 × 1 Monkhorst–Pack k-point grid with the cutoff energy of 85 Hartree was employed. The Pulaymixer algorithm controlled the self-consistent iterations with 0.0002 Ry tolerance and 100 maximum steps. The structures were optimized to a maximum force of 0.05 eV $Å^{-1}$ and the maximum stress of 0.005 eV $Å^{-3}$ with a limited memory Broyden–Fletcher–Goldfarb–-Shanno algorithm.[2] Based on these conditions, the corresponding optimization of M (MoO_2, MoP, MoO_2-MoP) slabs was constructed with a vacuum region of 15 Å on z-direction. The differential binding energy is used to describe the stability of hydrogen, defined as

$$\Delta E_H = E\ (M + nH) – E(M + (n\text{-}1)H – 1/2E(H_2)$$

where E (M + nH) is the total energy for the M slab adsorbed n hydrogen atoms, E(M + (n-1)H) is the total energy for (n-1) adsorbed hydrogen atoms on the M slab, and $E(H_2)$ is the energy of a gas phase hydrogen molecule. The Gibbs free energy ΔG_H for hydrogen adsorption can be calculated as

$$\Delta G_H = \Delta E_H + \Delta ZPE - T\Delta S_H$$

where ΔZPE is the zero-point energy difference between the adsorbed state of the system and the gas phase state, ΔS_H is the entropy difference between the adsorbed state of the system and the gas phase standard state (300 K, 1 bar).

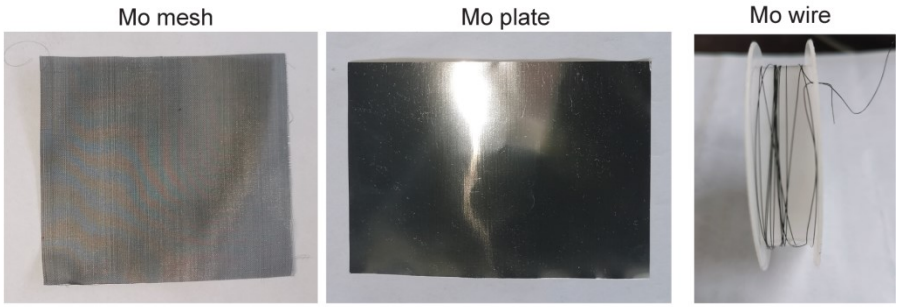

Fig. S1. Optical image of the (a) Mo mesh, (b) Mo plate, and (c) Mo wire.

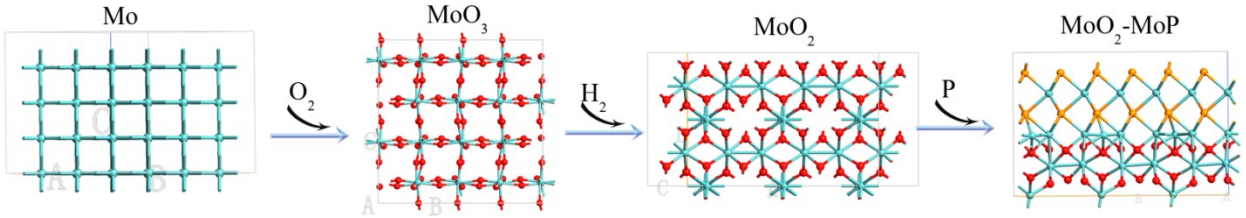

Fig. S2. Schematic of the fabrication process flow of MoO_2-MoP. A proposed growth process schematic of MoO_2-MoP from Mo by a CVD method can be explained in Supplementary Fig. 1. In the first step, a controlled oxidation reaction of Mo substrate in the air at 650 °C is used to grow MoO_3 on the Mo substrate surface. Subsequently, the MoO_3/Mo is subjected to a reduction in H_2 atmosphere at high temperature, obtaining the MoO_2/Mo. Note that this thermodynamical reduction process is critical to increasing the surface area and conductivity of the fabricated electrode. Finally, the surface of MoO_2 phosphide up to a point, forming the MoO_2-MoP. This easily obtained heterostructure can be ascribed to the surface oxygen atoms could be quickly taken out and substituted by phosphorus atoms.

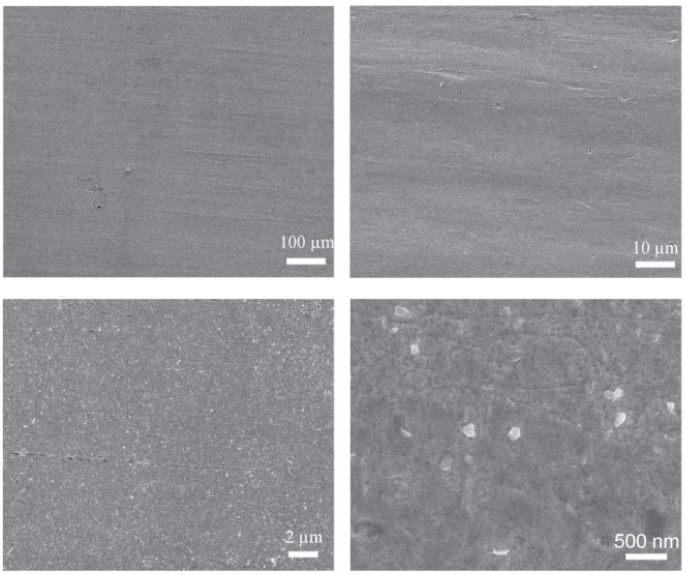

Fig. S3. SEM characterization of the pristine Mo plate. The surface morphology of the samples is characterized by SEM. Fig. S3 shows the surface morphology of the Mo plate, which exhibits a smooth surface.

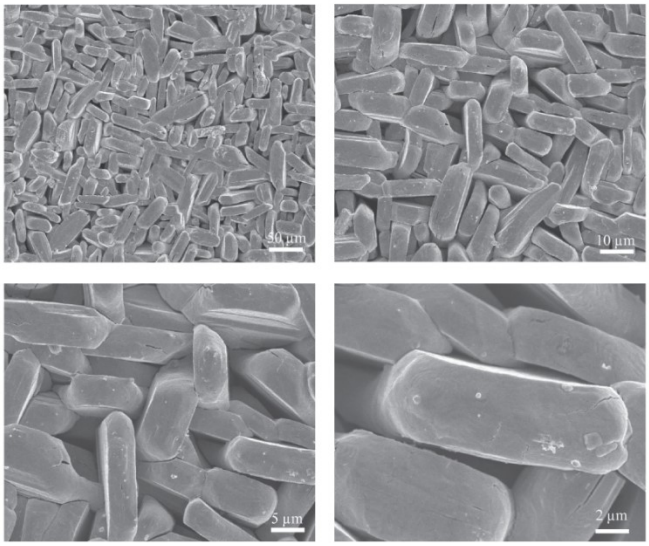

Fig. S4. SEM characterization of the obtained MoO_3. Fig. S4 shows the SEM images of MoO_3 grown on the surface of the Mo plate. The smooth surfaces of the Mo plate (Fig. S3) convert into prism-like MoO_3 crystals by annealing in the air. There are dense randomly distributed prisms with sizes in the range of ~1-2 µm and lengths of tens of microns are in-situ formed on the Mo plate. The magnified SEM images clearly show that the MoO_3 prisms exhibit a smooth surface.

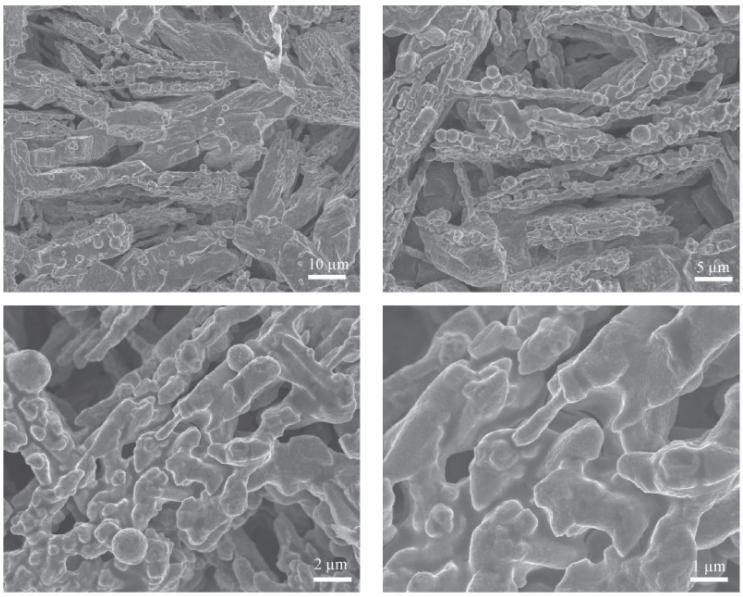

Fig. S5. SEM characterization of the obtained MoO_2. After the annealing of MoO_3 prisms in Ar and H_2 atmosphere, the as-obtained MoO_2 (Fig. S5) with a smaller size compared with MoO_3 prisms still preserve the prism-like morphology. Meanwhile, the magnified SEM images reveal that the prisms are composed of numerous stacked coarse flakes with a macroporous framework structure. Particularly, the MoO_2/Mo substrate is suitably employed as a current collector due to its high surface area, commercial availability, and good conductivity. Considering these promising physicochemical properties, it is expected that MoO_2 can be used to construct unique heterostructures for new interfaces, which is beneficial for catalytic activity.

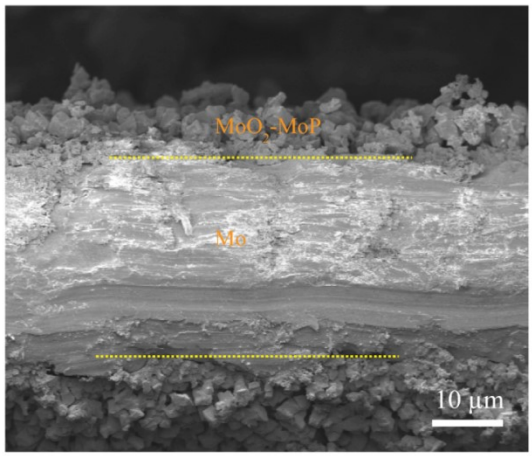

Fig. S6. The cross-sectional SEM image of MoO_2-MoP SE. The cross-sectional lamella of the MoO_2-MoP SE is shown in Fig. S6, in which MoO_2-MoP vertically growth is seen on a Mo substrate.

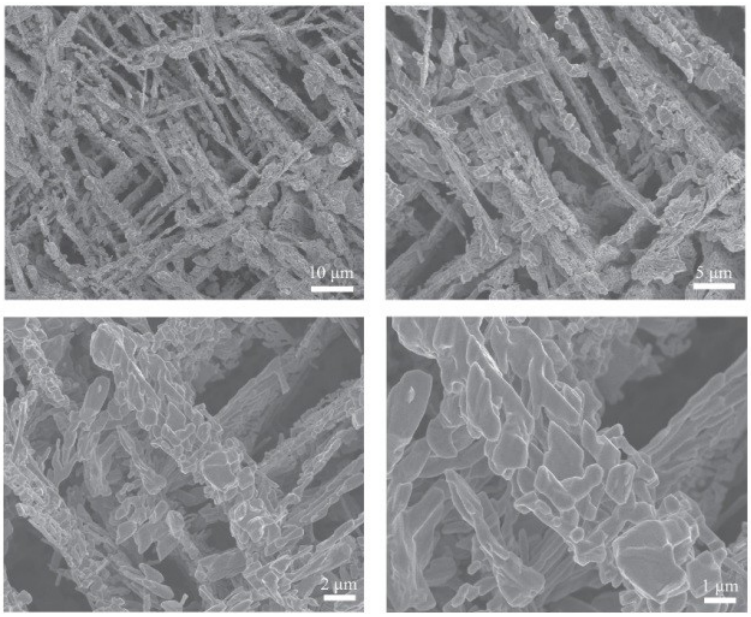

Fig. S7. SEM characterization of the obtained MoO_2-MoP SE. The magnified SEM images clearly show that the prisms are composed of many randomly oriented convex MoO_2-MoP flakes. The macroporous framework structure not only exposes more active sites for HER reaction but also facilitates the hydrogen bubbles release from the catalyst surface because of weak gas-solid interface adhesion, which is critical for HER at high current densities.

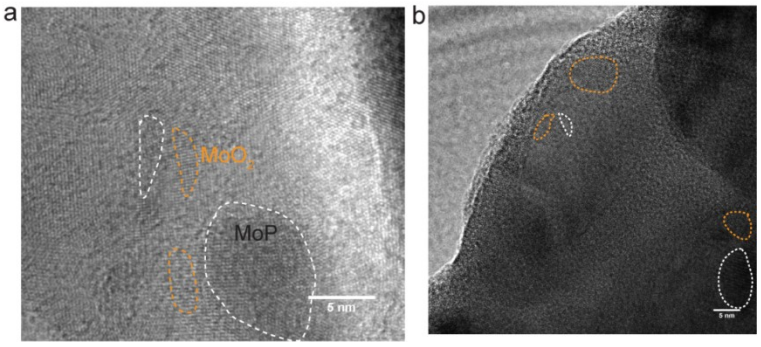

Fig. S8. TEM characterization of the obtained MoO_2-MoP. Clearly, the high-resolution TEM (HRTEM) images show intimate contact between MoP and MoO_2, revealing that MoP is an in-situ conversion from MoO_2 by phosphorization as illustrated in Fig. S8. In the CVD phosphorization process, partial O atoms in MoO_2 are attacked by hydrogen species, followed by phosphorization in which PH_x combines with the Mo atom to form the MoP phase.

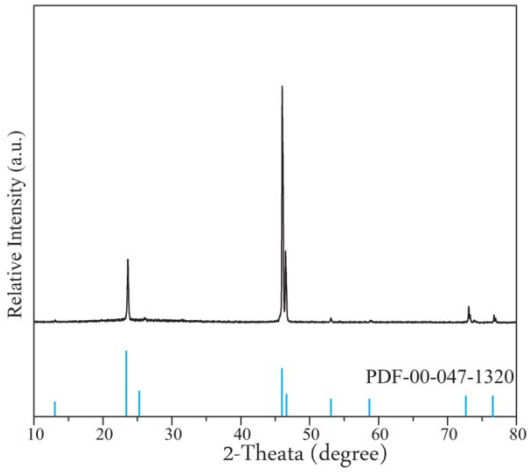

Fig. S9. The XRD pattern of the MoO_3 when the Mo plate is heated for 1 h at 650 ºC in air.

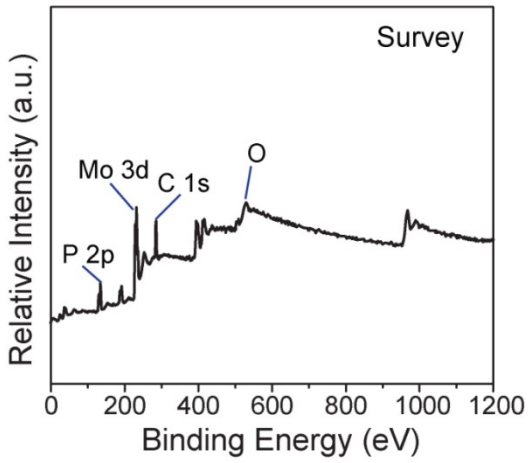

Fig. S10. XPS survey of MoO_2-MoP.The XPS analysis is carried out to probe the chemical compositions and surface valence states of the MoO_2-MoP. As illustrated in Fig. S9, the XPS spectrum confirms the presence of Mo, P, and O.

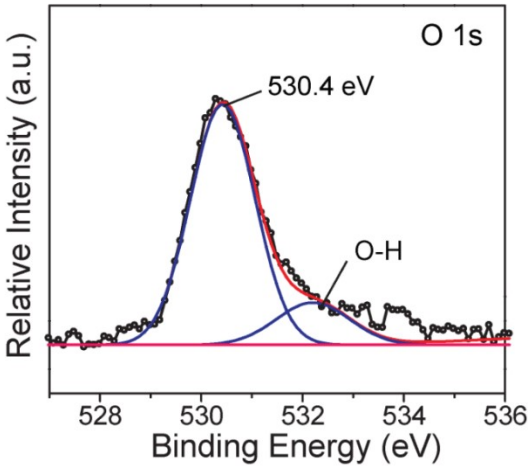

Fig. S11. XPS survey of O1s. The O 1s XPS peak at 530.4 eV corresponds to MoO_2 in $Mo_{(IV)}$-O bonds, which proves that MoO_2 has not been completely phosphide. The peak at 532.5 eV results from the inevitable surface oxidation of MoO_2-MoP upon exposure to air.

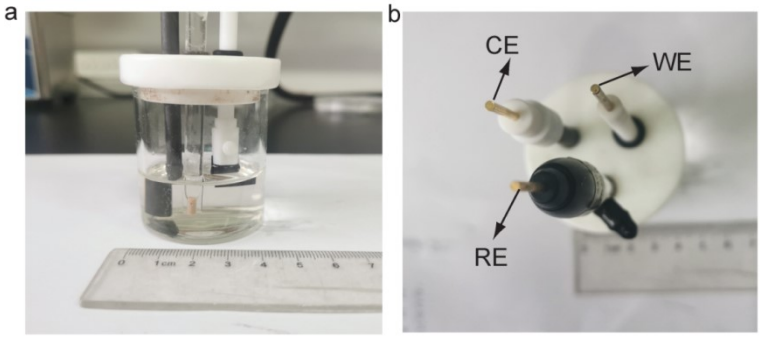

Fig. S12. Photos of the electrolysis cell for performing electrochemical tests. (a) Photos showing the size of the electrolysis cell. (b) Photos showing the positions and distances between working, counter, and reference electrodes.

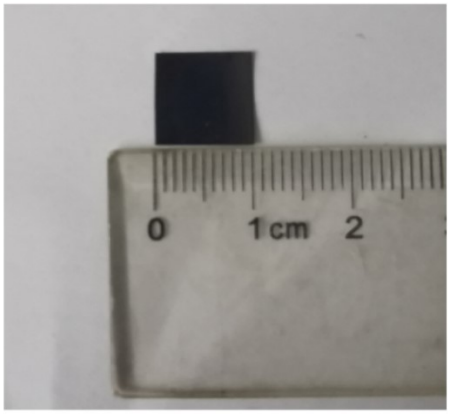

Fig. S13. A photo of a MoO_2-MoP working electrode. It shows an apparent surface area of 1.0×1.0 cm^2.

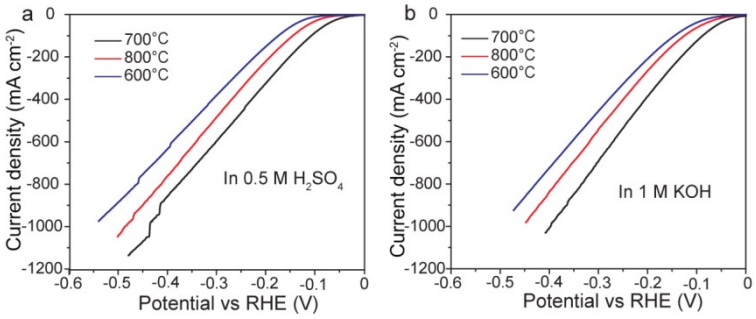

Fig. S14. Optimization of the HER performance of the MoO_2-MoP SE. The electrochemical measurements are performed in 0.5 M H_2SO_4 and 1.0 M KOH solution using a three-electrode electrochemical setup (see Methods for details). HER activities of MoO_2-MoP SE are optimized by controlling the phosphorization temperature. MoO_2-MoP SE is grown at the optimal growth condition at 700 °C.

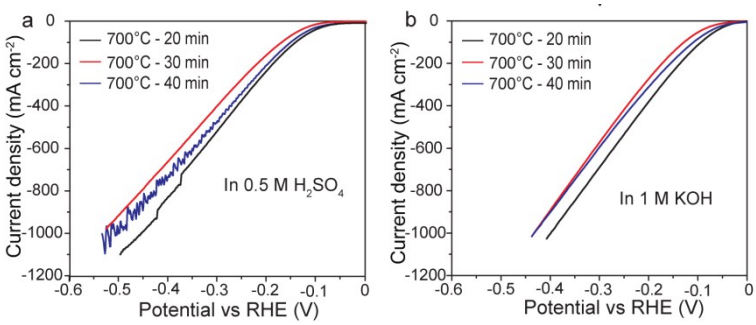

Fig. S15. The polarization curves of MoO_2/Mo phosphate at different times.

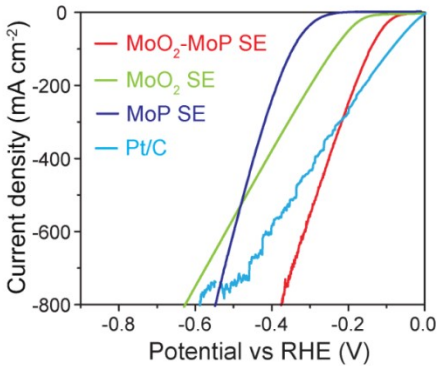

Fig. S16. HER polarization curves of MoO_2, MoP, MoO_2-MoP SE, and benchmark commercial Pt/C electrode in 0.5 M H_2SO_4 solution.

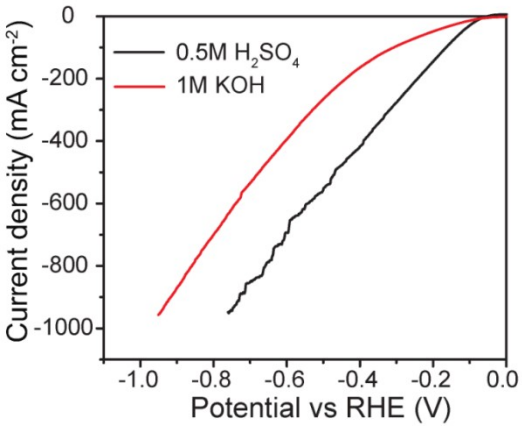

Fig. S17. The pH-universal HER performances of the Pt foil. The results show that Pt foil has good performance in both acidic and alkaline media**.**

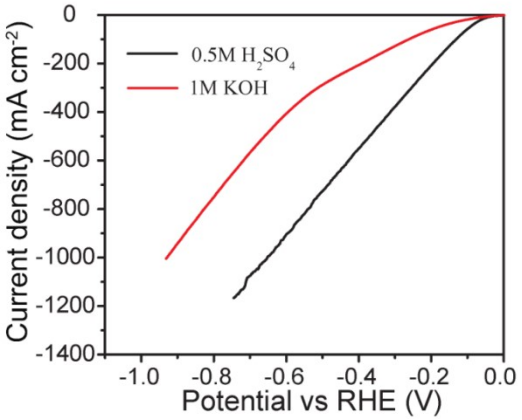

Fig. S18. The pH-universal HER performances of the Pt mesh. The results show that Pt mesh has good performance in both acidic and alkaline media**.**

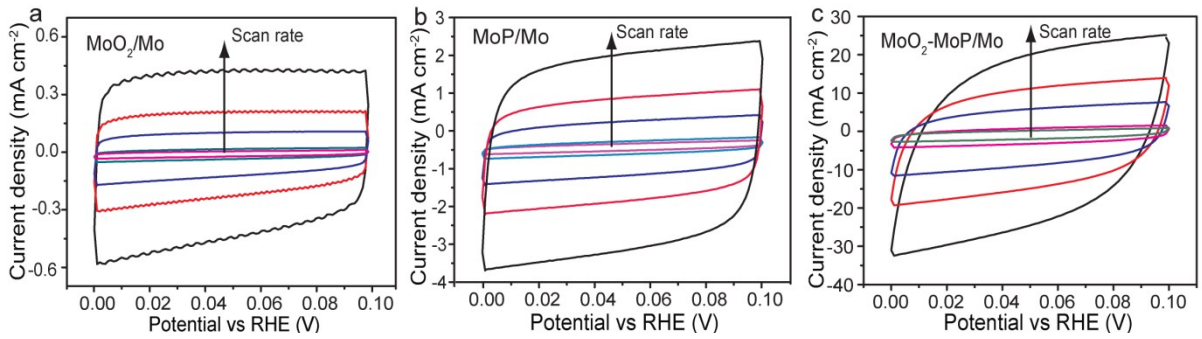

Fig. S19. CV curves at different scan rates and the calculated C_{dl}. The C_{dl} of the MoO_2, MoP, and MoO_2-MoP SE are assessed utilizing a series of cyclic voltammetry (CV) cycles at different scan rates. Cyclic voltammograms at different scan rates in the region between 0 and 0.1 V (vs. RHE) are recorded: (a) MoO_2, (b) MoP, and (c) MoO_2-MoP SE.

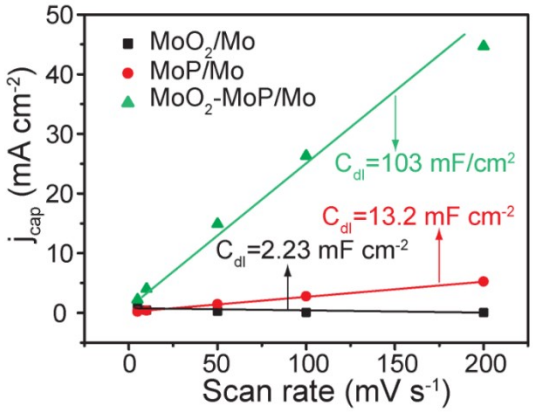

Fig. S20. Double-layer capacitance measurements for determining electrochemically active surface areas of MoO_2, MoP, and MoO_2-MoP SE. To clarify the influence of the active surface area on the electrocatalytic HER activity, the corresponding electrochemical double-layer capacitances (C_{dl}) of the electrocatalysts are analyzed by applying cyclic voltammetry cycles at different scan rates. As shown in Fig. S17, MoO_2-MoP SE exhibits a high capacitance C_{dl} value up to 103 mF cm^{-2}, which is greater than that of the MoP (13.2 mF cm^{-2}) and MoO_2 (2.23 mF cm^{-2}). Hence, this result demonstrates that MoO_2-MoP SE has the highest catalytic sites among various samples.

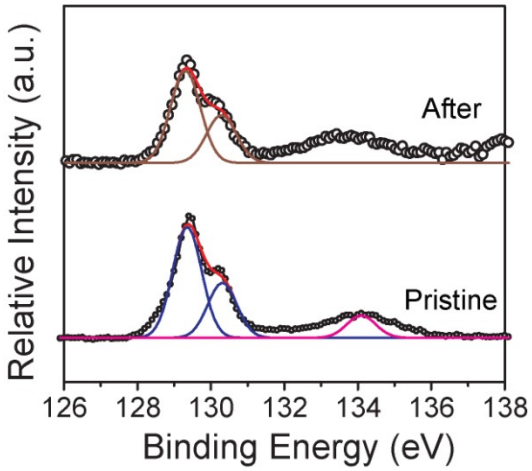

Fig. S21. XPS spectra of P 2p before and after stability test in alkaline media.

Fig. S22. OM characterization of MoO_2-MoP SE. Optical photograph of MoO_2-MoP SE and its flexibility.

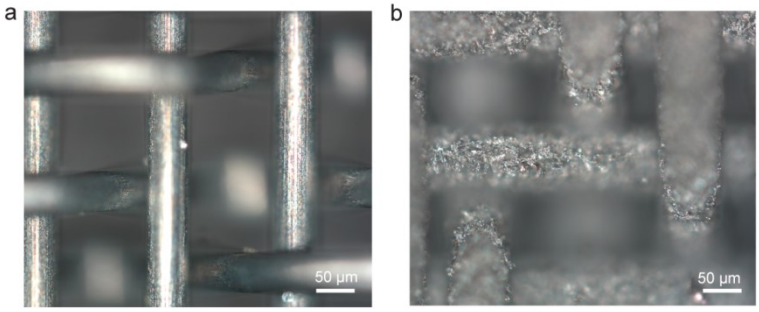

Figure S23. OM characterization. The OM images of (a) Mo mesh and (b) MoO_2-MoP mesh SE.

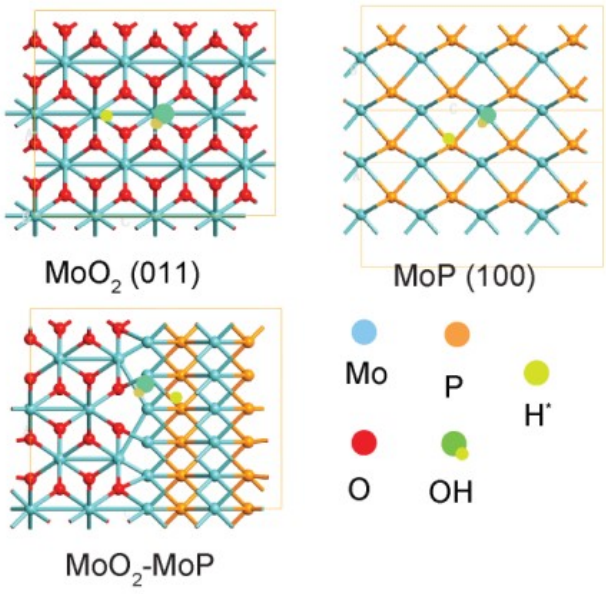

Fig. S24. Surface structure configurations of MoO_2, MoP, and MoO_2-MoP in the prior water-dissociation process.

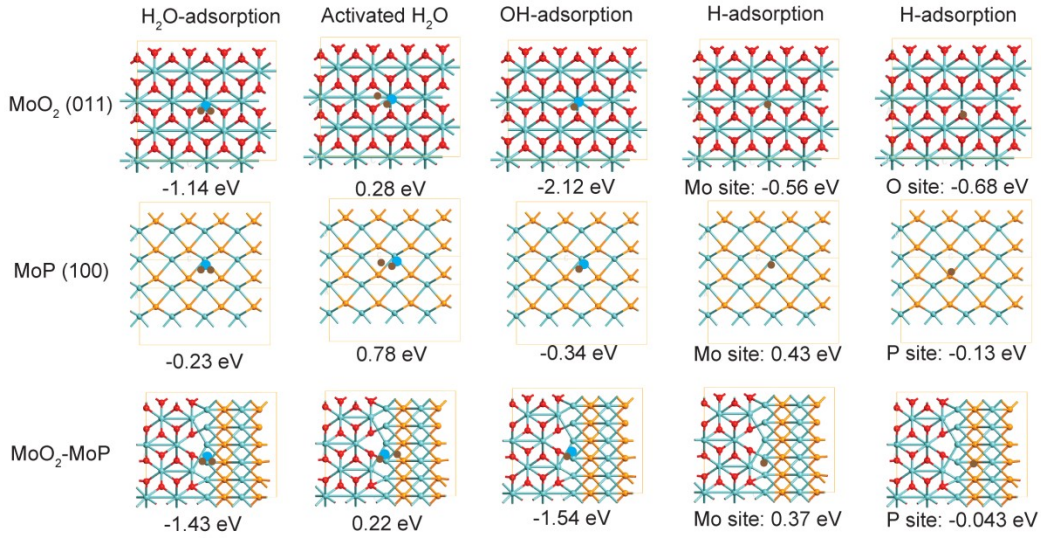

Fig. S25. Calculated free energies of H_2O adsorption, activated H_2O adsorption, OH adsorption, and H adsorption.

Tables S1. A comparison of the HER activity of the MoO_2-MoP SE in this work with previously reported data and our tested data of Pt-based catalysts.

Catalysts	**Electrolyte**	**Overpotential @ 1000 mA cm^{-2} (mV)**	**Reference**
MoO_2-MoP SE	KOH	383	This work
MoO_2-MoP mesh	KOH	293	This work
Pt/C	KOH	709	This work
Pt foil	KOH	998	This work
Pt mesh	KOH	973	This work
20 wt% Pt/C	KOH	415	18
Pt mesh	KOH	950	18
Pt foil	KOH	1180	18
Pt foil	KOH	822	12
Pt/C/Nafion	KOH	900	12
Pt wire	KOH	388	19

Table S2. The prices of the different metal substrates in this work.

Materials	Suppliers	Price per 1 m^2 (US$)	Thickness (cm)
Mo plate	Hebei Qingyuan Metallic Material Co. Ltd.	232	0.1
Mo mesh	Hebei Qingyuan Metallic Material Co. Ltd.	3000	0.1
Ni plate	Hebei Qingyuan Metallic Material Co. Ltd.	155	0.1
Ni mesh	Hebei Qingyuan Metallic Material Co. Ltd.	3000	0.1
Ti plate	Hebei Qingyuan Metallic Material Co. Ltd.	155	0.1
Ti mesh	Hebei Qingyuan Metallic Material Co. Ltd.	4500	0.1

References

S1 http://www.quantumwise.com/ for QuantumWise Atomistix ToolKit (ATK).

S2 N. Helbig, J. I. Fuks, M. Casula, M. J. Verstraete, M. A. L. Marques, I. V. Tokatly, and A. Rubio, *Phys. Rev. A*, **2011**, *83*, 032503.